Wireless Power Transfer

ARTICLE

Open Access

https://doi.org/10.48130/wpt-0026-0007

Wireless Power Transfer **2026**, 13: e019

Modeling and decoupling analysis for an integrated coupler and its non-compensated wireless power transfer system

Xueying Wu, He Li, Haisheng Wang, Xiaodong Qing, Qichang Feng and Zhengmei Lu*

School of Electronic and Electrical Engineering, Chongqing University of Science and Technology, Chongqing 401331, China

* Correspondence: luzmwork@cqust.edu.cn (Lu Z)

Abstract

A copper-foil electromagnetic coupler and its equivalent decoupled circuit model are developed in this paper to reduce the weight and cost of Wireless Power Transfer (WPT) systems, and improve system efficiency. The coupler consists of four stacked square spiral copper-foil coils, combining inductance and capacitance to enable the WPT system to function without the need for extra compensation components. The decoupled circuit model of the cross-coupling coils is analyzed and transformed equivalently. Through the design of structure and circuit parameters, the coupler achieves self-resonance. Besides, the conditions of both load-independent constant current or constant voltage output and input zero phase angle (ZPA) are given. The regularities of the electromagnetic coupling coefficient and system resonant frequency varying with the geometric parameters are obtained for system design and optimization. An experimental prototype is implemented and characterized. Under the operating conditions of 1.056 MHz and a 60-mm air-gap distance, measured performance yields an output power of 111.84 W, and a DC-DC conversion efficiency of 90.34%.

Keywords: Wireless power transfer (WPT), Electromagnetic coupling, Circuit analysis computing, Finite element method (FEM) simulation

Citation: Wu X, Li H, Wang H, Qing X, Feng Q, et al. 2026. Modeling and decoupling analysis for an integrated coupler and its non-compensated wireless power transfer system. *Wireless Power Transfer* 13: e019 https://doi.org/10.48130/wpt-0026-0007

Introduction

Combining advanced modeling and analysis methods, wireless power transfer (WPT) technology effectively addresses the issue of unsafe and inflexible access associated with conventional charging methods[1−5]. To increase the efficiency and power transfer capability of the WPT system, the existing research generally adopts two basic methods: improving the compensation structure and its parameter design method[6,7]; optimize the electromagnetic coupling structure[8,9]. The first method can raise the system output power, realize constant voltage or current output, suppress high-order harmonics, and reduce the reactive power component of the input. The second method has advantages in increasing the efficiency and power density, improving the misalignment ability, maintaining the system security, and reducing the system cost.

Four typical compensation topologies (S/S, S/P, P/S, and P/P) were utilized to improve the performance of inductive power transfer (IPT) systems, but they are prone to load sensitivity issues[10]. Regarding capacitive power transfer (CPT) systems, the coupler can be equivalent to two series coupling capacitors or six cross-coupling capacitors[11,12]. In centimeter-range power transmission applications, the method of using a large inductance for series reactive power compensation comes at the expense of system security and environmental adaptability[13]. In response to the challenges faced by IPT and CPT systems, a range of high-order compensation topologies, such as LCL (inductor capacitor inductor), LCC (inductor capacitor capacitor), CLC (capacitor inductor capacitor), and LCLC (inductor capacitor inductor capacitor), have been proposed. This paper presents a novel parameter tuning method based on an LCL compensation topology. The proposed approach provides enhanced flexibility in the design of IPT systems, along with improved suppression of higher-order harmonics and a reduction in coil current[14]. A dual-side LCC compensation topology along with its resonant scheme has been designed to ensure that the resonant frequency of the IPT system remains immune to variations in coupling coefficient and load, thereby maintaining stable and predictable operation[15]. A π-CLC compensation structure at the transmitter and T-CLC compensation structure at the receiver are adapted in the CPT system, which achieves constant current output when switching between multiple receivers[16]. To minimize the voltage stress imposed on the coupler to enable high-efficiency power delivery across long distances, a CPT system with double-sided LCLC compensation structure is put forward[17]. To continuously improve WPT system performance, scientists have carried out in-depth studies on electromagnetic coupling structures. A significant amount of focus has been placed on the development of a hybrid inductive and capacitive WPT (HWPT) system[18]. A novel HWPT system is presented that achieves a favorable trade-off between enhanced efficiency and a compact coupler design[19]. In addition, an inductive and capacitive integrated coupler, made up of bent aluminum plates, is introduced[20], offering a novel concept and approach for wireless charging. A 10 kW HWPT system exhibits a significant performance advantage, outperforming both previously published IPT and CPT systems across a range of misalignment conditions[21]. However, all of the above couplers have to be compensated by high-order network. In general, the magnetic-field coupler is typically constructed from Litz wire, whereas the electric-field coupler is composed of metal plates. To enhance performance, Litz wire, metal plates, and high-order compensation topologies are often incorporated. However, this approach comes at the expense of greater volume, weight, and cost, creating a critical barrier for WPT technology's progress and market adoption. In conclusion, the majority of existing research has focused on enhancing the output power, the efficiency, and the transfer distance of WPT systems, while neglecting the concomitant increases in volume, weight, and cost.

Aimed at resolving the problems outlined previously, this study puts forward a novel integrated copper-foil electromagnetic coupler and a comprehensive methodology for its modeling and decoupling. Fabricated from copper foil, the four planar square spiral coils that constitute the electromagnetic poles are designed with the objective of alleviating the skin effect, consequently minimizing

https://doi.org/10.48130/wpt-0026-0007

ohmic losses. Cross-coupling is generated among the four copper-foil coils; consequently, mutual inductances and cross-coupling capacitors are established. Compared with the previous research work, the proposed hybrid electromagnetic coupler is very lightweight and low cost, and the WPT system is very simple and practical for electric vehicle. The remainder of this paper is organized into the following sections. This paper first introduces the coupler structure and its decoupled model. The equivalent circuit of the coupler is analyzed and simplified, and the couplers' inherent electrical parameters are designed to make it self-resonance. Then the working conditions of both load-independent constant current (CC) or constant voltage (CV) output and input ZPA are obtained. In the following, the structure of the coupling electromagnetic pole is optimally designed based on Maxwell to balance the electric field and the magnetic field, and an efficient and portable electromagnetic coupler is constructed. Simulation and experimental results validating the proposed coupler and WPT system are discussed in verification part, concluding with the findings in the end.

Coupler structure, circuit modeling, and self-resonant principle

Copper-foil electromagnetic coupler

As shown in Fig. 1, the electromagnetic poles of the proposed coupler take the form of square spiral windings fabricated from copper foil. By leveraging the previously ignored parasitic capacitance of the coil, a significant improvement in power transmission performance can be achieved. Under the influence of both electric and magnetic fields, this coupler inherently integrates a combination of self-inductance, mutual inductance, and cross-coupling capacitor. The three-dimensional model of the copper-foil electromagnetic coupler is presented in Fig. 1a. Its key components are four planar square spiral electromagnetic poles and an insulating dielectric layer. Figure 1b depicts the front view of the copper-foil electromagnetic coupler, where the four electromagnetic poles and insulating dielectrics are stacked. Electromagnetic pole P_1, dielectric D_1, electromagnetic pole P_2, electromagnetic pole P_4, dielectric D_2, and electromagnetic pole P_3 are lined successively from bottom to top. l_1 is the side length of P_1 and P_3, while l_2 is the side length of P_2 and P_4. d_t and d_s are the transfer distance and the distance between the same-side electromagnetic poles (also the thickness of the dielectric), respectively.

System circuit topology and its equivalent simplification

With a view to structural simplification, this WPT system deliberately omits any additional compensation components. The copper-foil electromagnetic coupler utilizes its inherent capacitance and inductance characteristics to achieve self-resonant. A schematic illustration of the non-compensated circuit configuration is achieved in Fig. 2, where leakage field reduction is achieved by connecting the inner electromagnetic pole P_2 to the inverter's high-potential output terminal and the outer electromagnetic pole P_1 to the low-potential output terminal[23]. For simplicity, the circuit characteristics are analyzed employing the Fundamental Harmonic Approximation (FHA), with ohmic losses in the coupler omitted. Due to the equivalence between the six-capacitor cross-coupling and three-capacitor π-type models[24], the circuit from Fig. 2 can be simplified as depicted in Fig. 3, where $U_{\rm in}\,(U_{\rm in}=U_{\rm dc}\cdot 4/\pi)$ and $R_{\rm eq}\left(R_{\rm eq}=R_L\cdot 8/\pi^2\right)$ are defined as the inverter's fundamental output voltage component and the equivalent AC load resistance, respectively. The parameters in Figs 2 and 3 satisfy the following equivalent transformation relationship:

$$\begin{aligned} C_M &= \frac{C_{13}\cdot C_{24}-C_{13}\cdot C_{24}}{C_{23}+C_{24}+C_{13}+C_{14}} \\ C_1 &= C_{12}-C_M+\frac{(C_{13}+C_{14})\cdot(C_{23}+C_{24})}{C_{13}+C_{14}+C_{23}+C_{24}} \\ C_2 &= C_{34}-C_M+\frac{(C_{13}+C_{14})\cdot(C_{14}+C_{24})}{C_{13}+C_{14}+C_{23}+C_{24}} \end{aligned} \tag{1}$$

The electric field coupling coefficient is expressed as:

$$k_{\rm CPT}=\frac{C_M}{\sqrt{(C_1+C_M)\cdot(C_2+C_M)}} \tag{2}$$

According to the reciprocity theorem, the π-type capacitor network composed of C_1, C_2, and C_M can be transformed into a T-type capacitor network composed of C_A, C_B, and C_C. Furthermore, the multi-coupled inductor circuit can be equivalently represented as a controlled-source circuit, wherein the mutual inductance voltages are replaced by current-controlled voltage sources (CCVS). Figure 4 shows the equivalent circuit. The capacitors satisfy the following equations:

$$\begin{cases} C_A=C_1+C_M+\dfrac{C_1\cdot C_M}{C_2} & C_1=\dfrac{C_A\cdot C_B}{C_A+C_B+C_C} \\ C_B=C_1+C_2+\dfrac{C_1\cdot C_2}{C_M} & C_2=\dfrac{C_B\cdot C_C}{C_A+C_B+C_C} \\ C_C=C_2+C_M+\dfrac{C_2\cdot C_M}{C_1} & C_M=\dfrac{C_A\cdot C_C}{C_A+C_B+C_C} \end{cases} \tag{3}$$

Based on Kirchhoff's law, the input and output voltage can be expressed as:

$$\begin{cases} U_{\rm in}={\rm j}\omega L_2I_1+{\rm j}\omega M_{21}I_1+{\rm j}\omega(M_{23}+M_{24})I_2 \\ \qquad +U_{\rm AB}+{\rm j}\omega L_1I_1+{\rm j}\omega M_{12}I_1+{\rm j}\omega(M_{13}+M_{14})I_2 \\ U_{\rm aa}=-[{\rm j}\omega L_2I_2+{\rm j}\omega(M_{41}+M_{42})I_1+{\rm j}\omega M_{34}I_2+U_{\rm BC}] \\ \qquad -[{\rm j}\omega L_3I_2+{\rm j}\omega(M_{31}+M_{32})I_1+{\rm j}\omega M_{34}I_2] \end{cases} \tag{4}$$

By substituting I_1-I_3 for I_2, the input voltage can be simplified as:

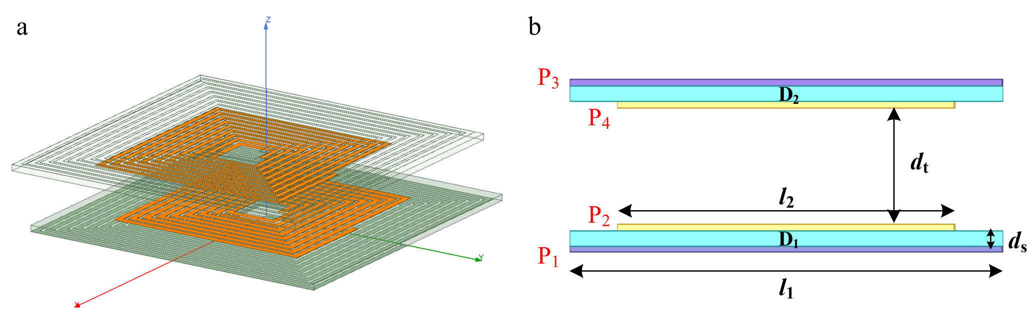

Fig. 1 Basic structure of the copper-foil electromagnetic coupler. (a) 3D graph of the coupler. (b) Front view[22].

https://doi.org/10.48130/wpt-0026-0007

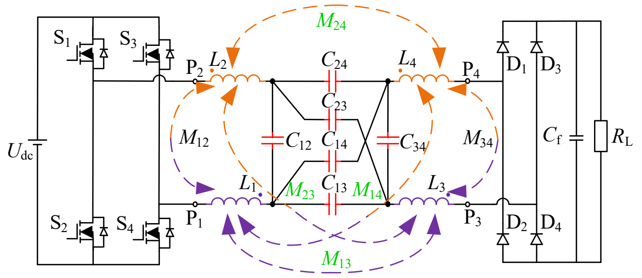

Fig. 2 Circuit topology of WPT system without compensation.

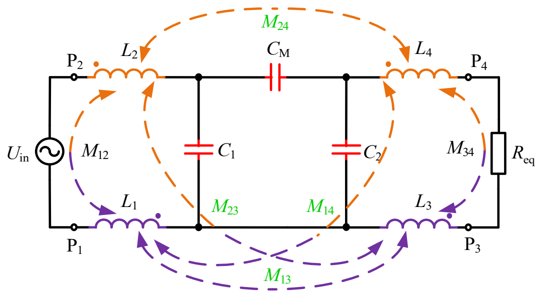

Fig. 3 System π-type equivalent model.

$$
\begin{aligned}
U_{\mathrm{in}} &= \mathrm{j}\omega I_1(L_2 + M_{21} + M_{23} + M_{24} + I_1 + M_{12} + M_{13} + M_{14}) \\
&\quad + \mathrm{j}\omega I_3(-M_{13} - M_{14} - \mathrm{M}_{23} - \mathrm{M}_{24}) + U_{\mathrm{AB}} \\
&= \mathrm{j}\omega I_1(L_{2\mathrm{M}} + L_{1\mathrm{M}}) + \mathrm{j}\omega I_3 L_{1\mathrm{M}} + U_{\mathrm{AB}}
\end{aligned} \tag{5}
$$

By substituting $I_2 + I_3$ for I_1, the output voltage can be simplified as:

$$
\begin{aligned}
U_{\mathrm{out}} &= -\mathrm{j}\omega I_2(L_4 + M_{41} + M_{42} + M_{43} + L_3 + M_{31} + M_{32} + M_{34}) \\
&\quad + \mathrm{j}\omega I_3(-M_{41} - M_{42} - M_{31} - \mathrm{M}_{32}) + U_{BC} \\
&= \mathrm{j}\omega I_2(L_{4\mathrm{M}} + L_{3\mathrm{M}}) + \mathrm{j}\omega I_3 L_{3\mathrm{M}} + U_{\mathrm{BC}}
\end{aligned} \tag{6}
$$

where,

$$
\begin{aligned}
L_{\mathbf{M}} &= -M_{13} - M_{14} - M_{23} - M_{24} \\
L_{\mathbf{1M}} &= L_1 + M_{12} + M_{13} + M_{14} \\
L_{\mathbf{2M}} &= L_2 + M_{21} + M_{23} + M_{24} \\
L_{\mathbf{3M}} &= L_3 + M_{31} + M_{32} + M_{34} \\
L_{\mathbf{4M}} &= L_4 + M_{41} + M_{42} + M_{43}
\end{aligned} \tag{7}
$$

In this paper, the magnetic-field coupling coefficient is conceptualized as:

$$
k_{\mathrm{IPT}} = \frac{L_{\mathbf{M}}}{\sqrt{(L_{\mathbf{M}} + L_{\mathbf{1M}} + L_{\mathbf{2M}})(L_{\mathbf{M}} + L_{\mathbf{3M}} + L_{\mathbf{4M}})}} \tag{8}
$$

which is used to describe the magnetic coupling degree between coils.

Circuit decoupled and parameter self-compensation

According to Eqs (5) and (6) in system circuit topology and its equivalent simplification, the controlled source circuit shown in Fig. 4 can be decoupled as a T-type model shown in Fig. 5. All inductances and capacitors are independent of each other. The simplified circuit can be divided into three impedance stages.

Based on the AC impedance method, the impedances at each stage depicted in Fig. 5 can be expressed as:

$$
\begin{aligned}
Z_1 &= \frac{1}{\mathrm{j}\omega C_{\mathrm{c}}} + \mathrm{j}\omega(L_{\mathbf{4M}} + L_{\mathbf{3M}}) + R_{\mathrm{eq}} \\
Z_2 &= \frac{Z_1 \cdot \left(\dfrac{1}{\mathrm{j}\omega C_{\mathrm{B}}} + \mathrm{j}\omega L_{\mathbf{M}}\right)}{Z_1 + \dfrac{1}{\mathrm{j}\omega C_{\mathrm{B}}} + \mathrm{j}\omega L_{\mathbf{M}}} \\
Z_{\mathrm{in}} &= Z_2 + \frac{1}{\mathrm{j}\omega C_{\mathrm{A}}} + \mathrm{j}\omega(L_{\mathbf{2M}} + L_{\mathbf{1M}})
\end{aligned} \tag{9}
$$

For practical implementations, the electromagnetic coupler is often deliberately designed to be symmetric, specifically featuring identical dimensions between pole pairs P_1 and P_3, or alternatively, P_2 and P_4. Furthermore, the distance between P_1 and P_2 is equal to the distance between P_3 and P_4. Therefore, the circuit parameters in Fig. 1b have the following relationship:

$$
\begin{cases} C_{12} = C_{34} \\ C_{14} = C_{23} \end{cases} \quad \begin{cases} L_1 = L_3 \\ L_2 = L_4 \end{cases} \quad \begin{cases} M_{12} = M_{34} \\ M_{14} = M_{23} \end{cases} \tag{10}
$$

According to Eqs (1), (3), and (6), the parameter relationships can be simplified as:

$$
\begin{cases} C_1 = C_2 \\ C_A = C_C = C_1 + 2C_{\mathbf{M}} \end{cases} \qquad \begin{cases} L_{\mathbf{1M}} = L_{\mathbf{3M}} \\ L_{\mathbf{2M}} = L_{\mathbf{4M}} \end{cases} \tag{11}
$$

According to Eqs (3) and (11), the electric-field coupling coefficient k_{CPT}, and magnetic-field coupling coefficient k_{IPT} shown in Eqs (2) and (8) can be re-expressed as:

$$
\begin{cases} k_{\mathrm{CPT}} = \dfrac{C_A}{C_A + C_B} \\ k_{\mathrm{IPT}} = \dfrac{L_{\mathbf{M}}}{L_{\mathbf{M}} + L_{\mathbf{M}} + L_{\mathbf{2M}}} \end{cases} \tag{12}
$$

According to Eqs (9), (11), and (12), if the system works in the input ZPA condition, the imaginary part of the system input impedance should be equal to zero, so the parameters must satisfy one of the equations as follows:

$$
\omega^2 C_A C_B (L_{\mathbf{1M}} + L_{\mathbf{2M}} + L_{\mathbf{M}}) = C_A + C_B \tag{13}
$$

or

$$
\frac{2\omega^2 L_{\mathbf{M}} C_A C_B + 2\omega^2 C_A (L_{\mathbf{1M}} + L_{\mathbf{2M}})(C_A + C_B)}{2\omega^4 C_A^2 C_B (L_{\mathbf{1M}} + L_{\mathbf{2M}})(L_{\mathbf{1M}} + L_{\mathbf{2M}} + 2L_{\mathbf{M}}) + \omega^2 C_A^2 C_B R_{\mathrm{eq}}^2 + 2C_A + C_B} = 1 \tag{14}
$$

Considering the above two conditions, some system parameters can be solved, as shown in Table 1, where A, B, and C are expressed as follows:

$$
\begin{aligned}
A &= C_{\mathrm{A}}^2 C_{\mathrm{B}} (L_{1\mathrm{M}} + L_{2\mathrm{M}})(L_{1\mathrm{M}} + L_{2\mathrm{M}} + L_{\mathrm{M}}) \\
B &= C_{\mathrm{A}}^2 C_{\mathrm{B}} R_{\mathrm{eq}}^2 - 2C_{\mathrm{A}} C_{\mathrm{B}} L_{\mathrm{M}} - 2C_{\mathrm{A}} (L_{1\mathrm{M}} + L_{2\mathrm{M}})(C_{\mathrm{A}} + C_{\mathrm{B}}) \\
C &= 2C_{\mathrm{A}} + C_{\mathrm{B}}
\end{aligned} \tag{15}
$$

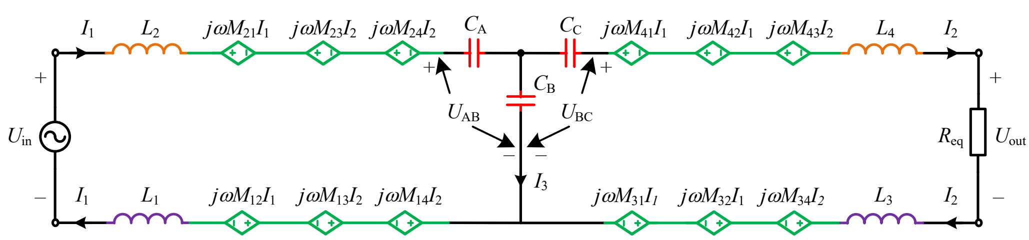

Fig. 4 Controlled source equivalent circuit.

https://doi.org/10.48130/wpt-0026-0007

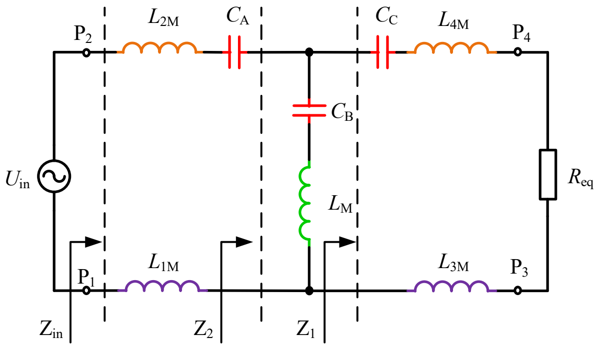

Fig. 5 System T-type decoupled model.

Since the current I_{out} is independent of R_{eq} under the first ZPA condition, the system operates in a CC output mode. For the second ZPA condition, the numerator and denominator of the output voltage U_{out} are conjugate complex numbers. The modulus of $\dot{U}_{out}$ can be expressed as:

$$\begin{aligned}\left|\dot{U}_{out}\right| &= \left|\dot{U}_{in}\right| \cdot \frac{\left|\omega^2 C_A(L_{1M}+L_{2M})-1+j\omega C_A R_{eq}\right|}{\left|\omega^2 C_A(L_{1M}+L_{2M})-1-j\omega C_A R_{eq}\right|} \\ &= \left|\dot{U}_{in}\right| \cdot \frac{\sqrt{(\omega^2 C_A(L_{1M}+L_{2M})-1)^2+\left(j\omega C_A R_{eq}\right)^2}}{\sqrt{(\omega^2 C_A(L_{1M}+L_{2M})-1)^2+\left(-j\omega C_A R_{eq}\right)^2}} = \left|\dot{U}_{in}\right|\end{aligned} \quad (16)$$

It means the system works in constant voltage (CV) output mode, while the phase of the output voltage is opposite to the input voltage.

Analysis and design of coupler parameters and circuit parameters

Analysis for the coupler parameters

Employing finite element analysis (FEA) in ANSYS Maxwell, the characteristics of the coupler were analyzed with various dimensions and its spatial structure optimized to improve system performance, with the planar rectangular spiral electromagnetic pole's top view provided in Fig. 6. The self-inductance of the planar square spiral coil is calculated based on the equation as follows:

$$L = \frac{1}{2}\mu_0 N^2 D_{avg} c_1 \left[\ln\left(\frac{c_2}{\rho}\right) + c_3\rho + c_4\rho^2\right] \quad (17)$$

where, μ_0, N, D_{avg}, and ρ are the vacuum permeability, turns of the coil, average value of inner and outer diameter of the coil ($D_{avg} = (D_{out}+D_{in})/2$), and compression ratio of the coil ($\rho=(D_{out}-D_{in})/(D_{out}+D_{in})$), respectively. The values of c_1–c_4 are determined by coil layout and shape. When the coil is square, c_1 = 1.27, c_2 = 2.07, c_3 = 0.18, and c_4 = 0.13.

In addition, the theoretical formula of a capacitor can be expressed as:

$$C = \frac{\varepsilon_0 \varepsilon_r S}{d} \quad (18)$$

where, ε_0 and ε_r are the permittivity of vacuum and the relative permittivity of dielectric. The coupling capacitor between any two electromagnetic poles is positively correlated with their copper area, while negatively correlated with the distance between them. In summary, the self-inductance, mutual inductance, and cross-coupling capacitor are mainly influenced by D_{out}, D_{in}, N, and w.

In practice, the outer diameter D_{out} of the electromagnetic pole is generally determined by the specific application occasion. In this section, the outer electromagnetic pole (P_1 and P_3) with the size of 500 * 500 mm (D_{out} = 500 mm) is used for research. According to Eq. (16), when D_{out} is given, the self-inductance of the outer pole is mainly related to its width of copper foil w_{out}, number of turns N_{out}, and turns spacing s_{out}. In addition to the aforementioned parameters, the mutual inductances and cross-coupling capacitors are also governed by the width of the copper foil winding of the inner electromagnetic pole, the number of turns N_{in}, the turn spacing s_{in}, the transmission distance d_t, and the inter-pole distance on the same side d_s.

Influence of the poles' turns

To achieve larger cross-coupling capacitors, Polymethyl methacrylate (PMMA, relative permittivity 3.4) is employed as the dielectric medium separating the electromagnetic poles on each side. The system parameters, as defined in Table 2, are adopted for this investigation.

Further analysis reveals the changing pattern of input impedance Z_{in} with respect to N_{in} and R_{eq}, as illustrated in Fig. 7[22]. It can be observed that Z_{in} is primarily determined by R_{eq}, but the variation with N_{in} is relatively small. When Req assumes a small value (10–100 Ω), Z_{in} becomes quite high, leading to a minimal amount of

Table 1. System parameters in two ZPA conditions.

System parameters	First ZPA condition	Second ZPA condition
Operating angular frequency	$\omega=\sqrt{\dfrac{C_A+C_B}{(L_{1M}+L_{2M}+L_M)C_A C_B}}$	$\begin{cases}\omega_1=\sqrt{\dfrac{-B+\sqrt{B^2-4AC}}{2A}} \\ \omega_2=\sqrt{\dfrac{-B-\sqrt{B^2-4AC}}{2A}}\end{cases}$
Input impedance	$Z_{in}=\dfrac{((L_{1M}+L_{2M})C_A-L_M C_B)^2}{(L_M+L_{1M}+L_{2M})(C_A+C_B)C_A C_B R_{eq}}$	R_{eq}
Output voltage	$\dot{U}_{out}=-j\dot{U}_{in}R_{eq}\dfrac{\sqrt{(L_M+L_{1M}+L_{2M})(C_A+C_B)C_A C_B}}{(L_{1M}+L_{2M})C_A-L_M C_B}$	$\dot{U}_{out}=-\dot{U}_{in}\cdot\dfrac{\omega^2 C_A(L_{1M}+L_{2M})-1+j\omega C_A R_{eq}}{\omega^2 C_A(L_{1M}+L_{2M})-1-j\omega C_A R_{eq}}$
Output current	$\dot{I}_{out}=-j\dfrac{\sqrt{(L_M+L_{1M}+L_{2M})(C_A+C_B)C_A C_B}}{(L_{1M}+L_{2M})C_A-L_M C_B}\dot{U}_{in}$	$\dot{I}_{out}=-\dfrac{\dot{U}_{in}}{R_{eq}}\dfrac{\omega^2 C_A(L_{1M}+L_{2M})-1+j\omega C_A R_{eq}}{\omega^2 C_A(L_{1M}+L_{2M})-1-j\omega C_A R_{eq}}$

https://doi.org/10.48130/wpt-0026-0007

Table 2. Parameters of the coupler when Nin is variable.

Parameter	Value	Parameter	Value
N_{out}	15	d_t	60 mm
s_{out}	5 mm	s_{in}	5 mm
d_s	10 mm	w_{out}	10 mm
w_{in}	10 mm		

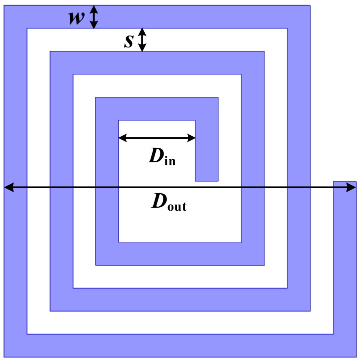

Fig. 6 Top view of the single coil.

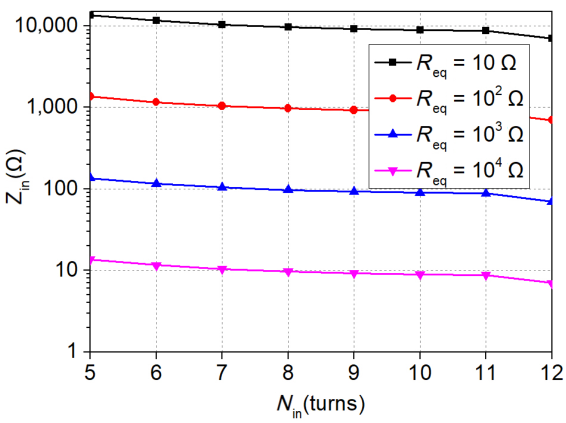

Fig. 7 Variation of the input impedance with N_{in} and R_{eq}[22].

power picked up at the load end. When R_{eq} takes on a large value (10^3–10^4 Ω), Z_{in} ranges from 10 to 100 Ω; however, under CV operating mode, the current picked up by the load remains quite small.

As derived from the preceding analysis, the first ZPA operating mode is exclusively suited for applications characterized by an exceptionally high equivalent load resistance and a minimal load current. Since most practical implementations feature load resistances below 100 Ω, this paper consequently examines the electromagnetic coupler's performance under the second ZPA condition for subsequent analysis and design.

With varying N_{in}, the self-resonance frequency of the coupler differs significantly, leading to distinct ground voltages of the four electromagnetic poles. The dependence of the ground-referenced voltage at P_3 and P_4 on N_{in} is examined under two distinct operating frequencies, f_1 and f_2, as depicted in Fig. 8[22]. A marked disparity is observed, with U_{P3} and U_{P4} demonstrating a substantial increase when the system operates at frequency f_2 compared to frequency f_1. Therefore, the selection of f_1 as the system operating frequency serves to reduce the coupler's fringing electric field and improve overall safety. Subsequent sections are dedicated to the analysis and design of a WPT system targeting operation at the resonant frequency $f = f_1$.

Based on the parameters listed in Table 2, the dependence of the self-inductances, mutual inductances, and cross-coupling capacitors of the four electromagnetic poles on N_{in} can be systematically investigated through Maxwell simulations. Then, the regularity of the magnetic-field coupling coefficient k_{IPT} and electric field coupling coefficient k_{CPT} changing with N_{in} is obtained as shown in Fig. 9. It can be seen that k_{IPT} is negative, which is related to the setting of the homonymous end of the coupling coil. The determination of the homonymous end is affected by the current direction in the coil, which is related to the winding mode of the coil.

Influence of the poles' width

With the parameters of the coupler listed in Table 3 held constant, the influence of the copper foil width on the system parameters is investigated. In order not to change the occupied area of the outer electromagnetic pole (15 turns, 500 * 500 mm), and the inner electromagnetic pole (nine turns, 330 * 330 mm), the sum of copper foil width and turns spacing in the table is fixed as 15 mm. If the copper foil width changes, the copper-foil turns spacing changes accordingly. Through parametric scanning analysis on Maxwell, The functional dependence of both the magnetic and electric field coupling coefficients on the geometric parameters (copper foil widths w_{in}/w_{out} or turn spacings s_{in}/s_{out}) is illustrated in the accompanying contour diagrams, as shown in Fig. 10. A clear correlation is observed whereby the absolute value of k_{IPT} correlates positively with both w_{in} and w_{out}, whereas k_{CPT} increases with larger w_{in} but decreases with larger w_{out}. Moreover, Fig. 11 shows the regularity of the first resonant frequency f_1 varying with w_{in} and w_{out} in the case of R_{eq} = 40 Ω. It is known that the self-inductances, mutual inductances, and cross-coupling capacitors of the electromagnetic poles increase with the increase of w_{in} and w_{out}, so the system resonance frequency decreases, as shown in Fig. 11.

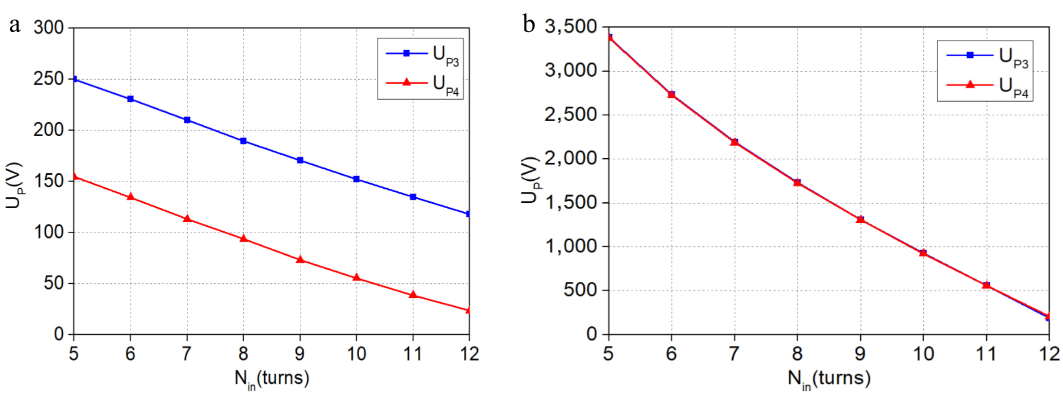

Fig. 8 Ground-referenced voltage curve of P_3 and P_4[22]. (a) $f = f_1$. (b) $f = f_2$.

https://doi.org/10.48130/wpt-0026-0007

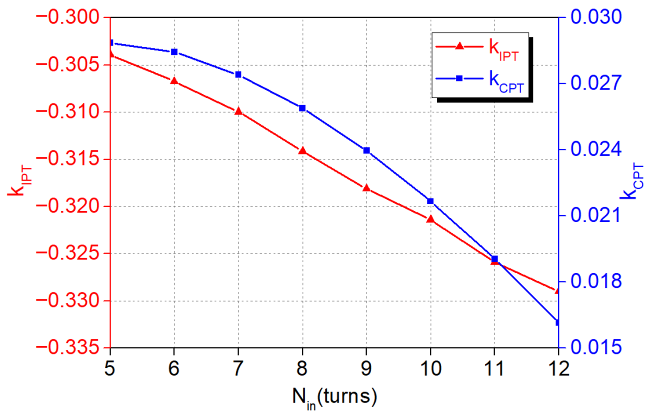

Fig. 9 Variation of magnetic-field and electric-field coupling coefficient.

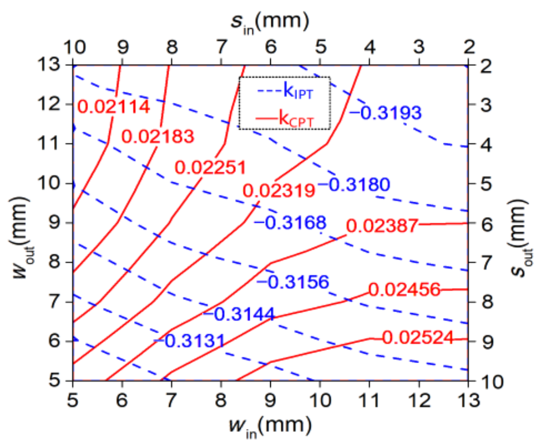

Fig. 10 The variation of coupling coefficient with w_{in} and w_{out} (or s_{in} and s_{out}).

Influence of same-side spacing and transfer distance

The transfer distance d_t and the same-side electromagnetic poles spacing are set as variables, and the other parameters shown in Table 4 are taken as invariants, then the three-dimensional curved surface of k_{IPT} and k_{CPT} varying with d_t and d_s can be obtained, as shown in Figs 12 and 13. With the increase of d_s, k_{CPT}, and the absolute value of k_{IPT} increase gradually. However, as d_t increases, k_{CPT} and the absolute value of k_{IPT} decrease gradually. Generally, the larger the coupling coefficient is, the more conducive to the power transmission. Therefore, it is crucial to carefully balance the relationship between the coupling coefficient and the volume of the coupler when designing the coupler for practical application, which involves selecting appropriate values for d_s and d_t.

Table 3. Parameters of the coupler when sout and wout are variable.

Parameter	Value	Parameter	Value
N_{out}	15	N_{in}	9
$s_{out} + w_{out}$	15 mm	d_t	60 mm
d_s	10 mm	$s_{in} + w_{in}$	15 mm

Table 4. Parameters of the coupler when d_s and d_t are variable.

Parameter	Value	Parameter	Value
N_{out}	15	N_{in}	9
s_{out}	5 mm	s_{in}	5 mm
w_{out}	10 mm	w_{in}	10 mm
R_{eq}	40 Ω		

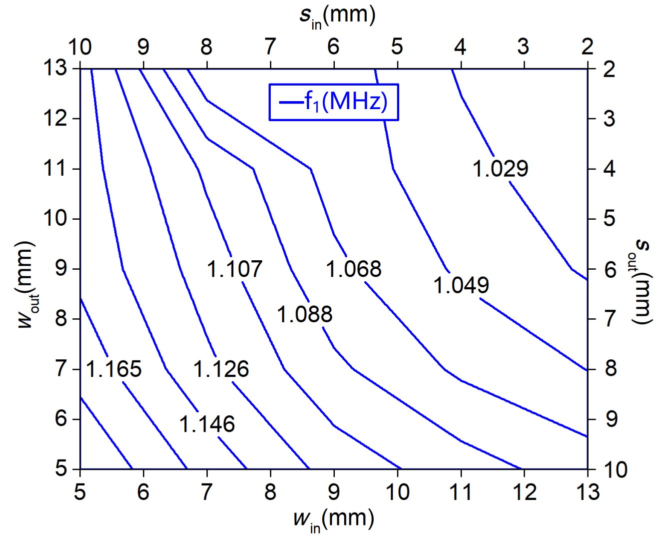

Fig. 11 The variation of the system resonance frequency f_1 with w_{in} and w_{out} (or s_{in} and s_{out}).

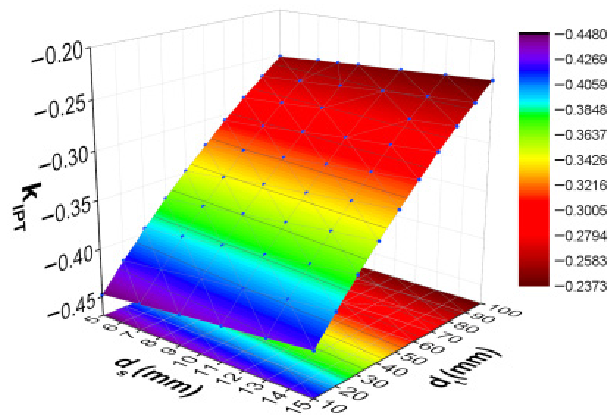

Fig. 12 The variation of k_{IPT} with d_s and d_t.

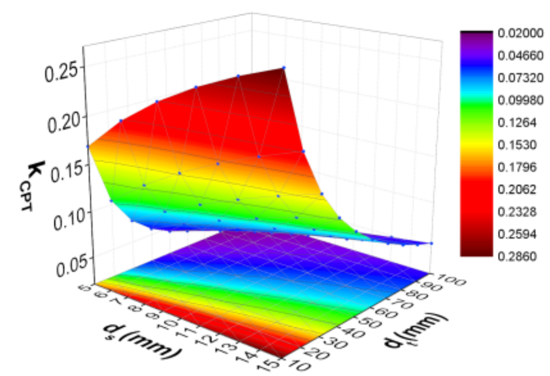

Fig. 13 The variation of k_{CPT} with d_s and d_t.

Moreover, the changes in self-inductance, mutual inductance, and cross-coupling capacitance with respect to d_s and d_t can also be obtained, leading to the derivation of the relationship between f_1 and d_s, as well as d_t, as illustrated in Fig. 14. As d_s and d_t increase, the mutual inductances and cross-coupling capacitances decrease, so the system resonance frequency increases.

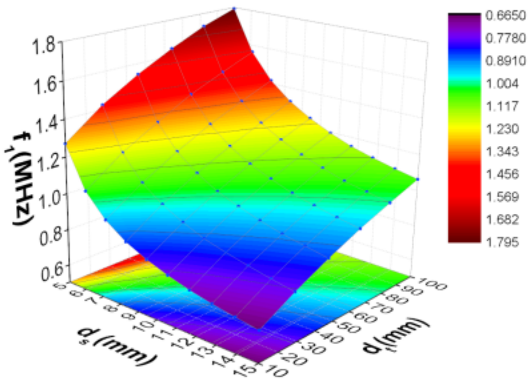

Fig. 14 The variation of f_1 with d_s and d_t.

Simulation and experimental verification

Parameters determination and simulation verification

According to the previous literature and experience, the frequency is generally around 1 MHz, so the value of inductance and capacitance will be less affected by the surrounding environment. In addition, the magnetic-field and electric-field coupling coefficient should be balanced, since they determine the system power transmission capability. To systematically optimize the coupler's geometry, the relationship between its parameters and the circuit parameters is investigated. Therefore, the self-inductances, mutual inductances, and cross-coupling capacitors can be obtained by Maxwell. Based on the above analysis in analysis and design of coupler parameters and circuit parameters, if the geometric parameters of the coupler are designed as in Table 5, the operation frequency equals 1.056 MHz, and the magnetic-field and electric-field coupling coefficients are calculated as −0.318 and 0.024, respectively. All the circuit parameters are shown in Table 6. Based on the circuit topology in Fig. 2, and the parameters in Table 6, the system simulation is conducted on MATLAB/Simulink.

The phase synchronization observed between the inverter output voltage and current in Fig. 15 confirms that the system achieves a unity input power factor by satisfying the ZPA condition. A measured input current amplitude of 2.484 A for the system compares well to the calculated value of 2.5 A. With a variable AC load, the system output voltage is presented in Fig. 16, which shows an acceptable constant voltage output. When the AC load R_{eq} increases by 100% (from 40 to 80 Ω), the output voltage increases by 0.4%. When R_{eq} decreases by 100% (from 40 to 20 Ω), the output voltage decreases by 1.36%. Table 7 shows the simulation voltages to ground of P_1–P_4 and the currents through them. P_1 and P_2 are directly connected with the output port of the inverter, so their amplitude values of the voltage to ground are equal to the inverter output voltage. The currents through P_1 and P_2 are equal, as well as the currents through P_3 and P_4, which can be also deduced from the structure shown in Fig. 2. According to IEEE human safety standard[25], the permissible levels for human exposure to electric and magnetic fields are defined by the operating frequency f_s in the following manner:

$$E_{\mathrm{RMS}} = \begin{cases} 614, & 0.1\ \mathrm{MHz} \le f_s < 1.34\ \mathrm{MHz} \\ 823.8/f_s, & 1.34\ \mathrm{MHz} \le f_s < 30\ \mathrm{MHz} \end{cases}$$
$$H_{\mathrm{RMS}} = 16.3/f_s, 0.1\ \mathrm{MHz} \le f_s < 30\ \mathrm{MHz} \tag{19}$$

where, E_{RMS} (V/m) and H_{RMS} (A/m) are the root mean square of the electric field strength and magnetic field strength, respectively. Taking the voltages and currents in Table 7 as the excitation sources, finite element analysis is conducted on ANSYS Maxwell, and the electric field and magnetic field around the coupler are obtained, as shown in Fig. 17a and b, where the safety distance is presented.

Table 5. Geometric parameters of the coupler.

Parameter	Value	Parameter	Value
N_{out}	15	N_{in}	9
s_{out}	5 mm	s_{in}	5 mm
w_{out}	10 mm	w_{in}	10 mm
d_s	10 mm	d_t	60 mm

Table 6. Circuit parameters for simulation.

Parameter	Value	Parameter	Value	Parameter	Value
f	1.056 MHz	M_{12}	22.731μH	C_{12}	324.98 pF
U_{dc} (U_{in})	78.54V (100 V)	M_{13}	28.369 μH	C_{13}	30.376 pF
R_L (R_{eq})	49.348 Ω (40 Ω)	M_{14}	12.367 μH	C_{14}	3.0998 pF
L_1	64.622 μH	M_{23}	12.366 μH	C_{23}	3.1395 pF
L_2	19.517 μH	M_{24}	7.2848 μH	C_{24}	13.198 pF
L_3	64.407 μH	M_{34}	22.722 μH	C_{34}	324.14 pF
L_4	19.432 μH				

Experimental results

Based on the WPT system in Fig. 2 and its equivalent circuit in Figs 3 and 5, the experimental prototype is built with the coupler's dimension parameters in Table 5, as shown in Fig. 18. The coupler is

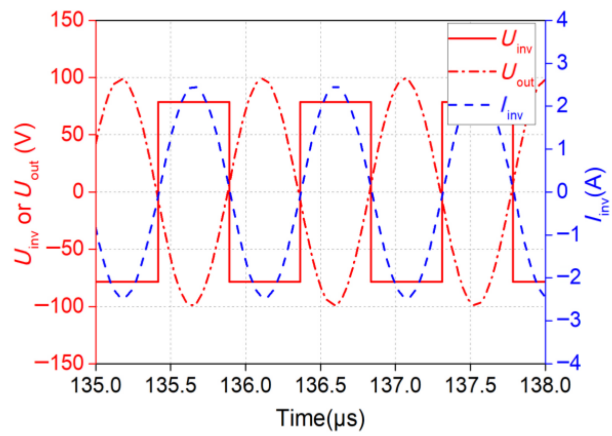

Fig. 15 Simulation waveforms of inverter output voltage and current.

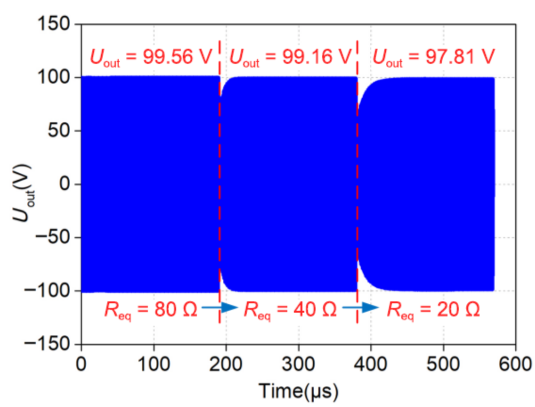

Fig. 16 Simulation waveforms of system output voltage varying with R_{eq}.

Table 7. Amplitude value of the voltage to ground and current of P_1–P_4.

Parameter	Value	Parameter	Value
$U_{P1\text{-}G}$	100 V	$U_{P2\text{-}G}$	100 V
$U_{P3\text{-}G}$	170.9 V	$U_{P4\text{-}G}$	72.24 V
I_{P1}	2.484 A	I_{P2}	2.484 A
I_{P3}	2.475 A	I_{P4}	2.475 A

made up of four square planar spiral copper-foil coils (P_1–P_4) arranged vertically. The copper foil strip is spirally wounded on the surface of acrylic plates. To reduce losses caused by skin effect, we should choose the copper foil with a suitable thickness. So the skin depth of the copper foil should be calculated, which can be expressed as:

$$\delta = \sqrt{\frac{1}{\pi\mu\sigma f}} \tag{20}$$

where, μ is the copper magnetic permeability and equals 4π × 10^{-7} H/m; σ is the copper conductivity and equals 5.8 × 10^7 S/m; f is the operating frequency, and the unit is Hz. When f = 1.056 MHz, δ = 64.3 μm, so the copper-foil thickness is approximately selected as 2δ for the experiment. The power transmitter is formed by P_1 and P_2 attached to D_1, while the power receiver is formed by P_3 and P_4 attached to D_2. The self-inductances, mutual inductances, and cross-coupling capacitors are measured using an Agilent E4980A LCR meter, with the results being closely aligned with the simulations in Table 6. The inverter incorporated Cree C2M0080120D SiC MOSFETs, with a TMS320F28335 DSP serving as the digital controller.

The experimental waveforms of the inverter output voltage, current, and AC load voltage are shown in Fig. 19 when the equivalent AC load resistance R_{eq} equals 40 Ω. The phase of the inverter output current I_{inv} lags the inverter output voltage U_{inv} slightly, which means the input impedance is weakly inductive and zero voltage switching (ZVS) condition is achieved. The phase difference between the inverter output voltage and current is defined as[16]:

$$|\theta| \geq \arcsin\frac{2C_{\text{oss}}U_{\text{in}}}{I_{\text{in}}t_D} \tag{21}$$

where, C_{oss} and t_D represent the parasitic output capacitance and the switching dead time, respectively. It is critical that is fully discharged prior to the transistor turn-on. Furthermore, the inverter output

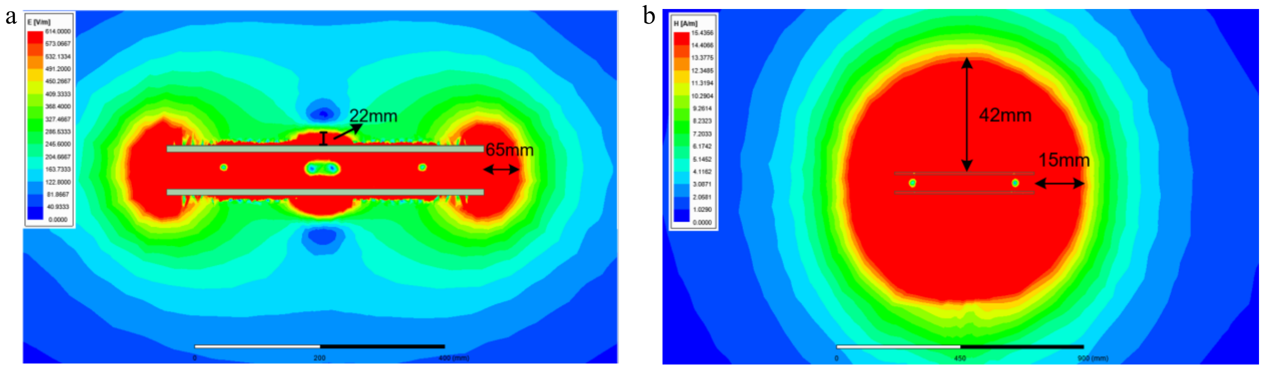

Fig. 17 (a) Electric field distribution around the coupler. (b) Magnetic field distribution around the coupler.

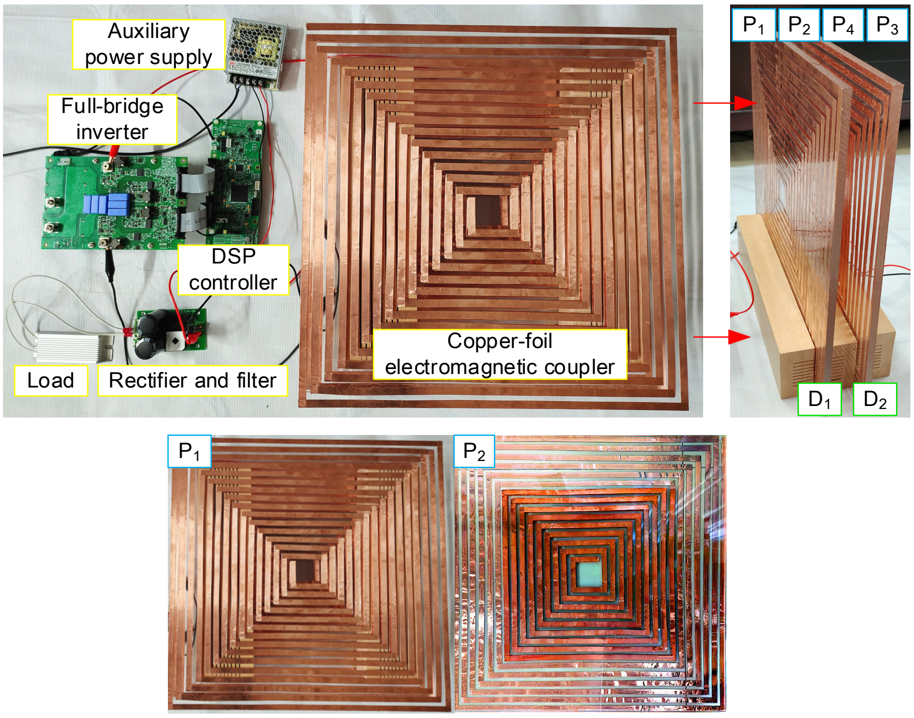

Fig. 18 Experimental prototype of the WPT system.

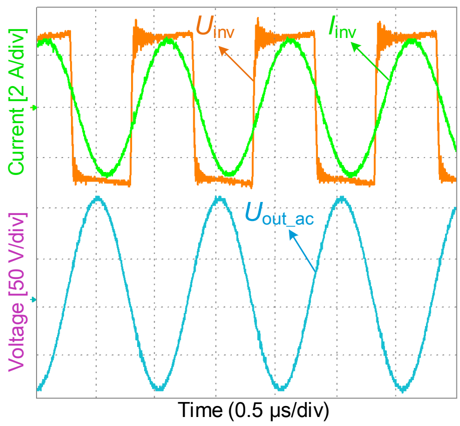

Fig. 19 Experimental waveforms of the inverter output and the AC load voltage.

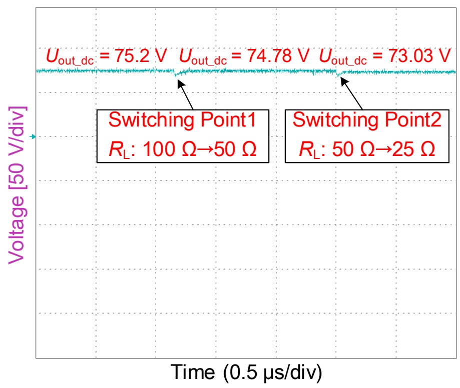

Fig. 20 Experimental waveforms of the DC load voltage when R_L changes (100→50→25 Ω).

voltage and the AC load voltage are 180° out of phase, while the fundamental component of U_{inv} is equal to U_{out_ac}, thereby validating the simulation results presented in Fig. 15. Figure 20 shows the experimental waveforms of the DC load voltage U_{out_dc} when R_L changes from 100 to 50 Ω, then to 25 Ω. With R_L increasing or decreasing 100%, U_{out_dc} changes within 2%, achieving an approximately constant voltage output under a wide load range. The experiment data are measured by a power analyzer when R_L equals 50 Ω, as shown in Fig. 21. The input power and output power are 123.83 and 111.84 W, respectively, so the system efficiency is 90.32%. The loss distributions of the experimental prototype are shown in Fig. 22. It can be seen that the system losses are dominated by the four copper-foil electromagnetic poles.

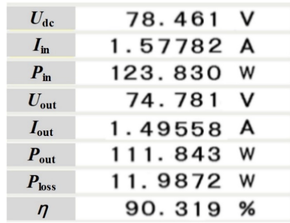

U_{dc}	78.461	V
I_{in}	1.57782	A
P_{in}	123.830	W
U_{out}	74.781	V
I_{out}	1.49558	A
P_{out}	111.843	W
P_{loss}	11.9872	W
η	90.319	%

Fig. 21 The experiment results shown in power analyzer.

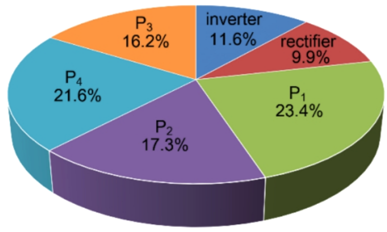

Fig. 22 Loss distributions of the experimental prototype.

The misalignment tolerance of the system was evaluated, and the corresponding results are presented in Fig. 23. It can be seen from the overall trend of change that the output power drops with the X or Y misalignment increasing. The system performance degrades significantly at a misalignment of 150 mm, with both output power and efficiency plummeting to around 30% of those achieved in the perfectly aligned state. When the misalignment increases to about 250 mm, the output power and efficiency are very low. But they rise slightly when the misalignment continues to increase. That's because, the coupling coefficients k_{CPT} and $|k_{IPT}|$ are very small when the misalignment is in the range of (250, 300 mm), and only a little electric power can be transmitted. With the continuous increase of the misalignment, k_{CPT} and $|k_{IPT}|$ return to increase slightly, but both of them are going to end up near zero.

Conclusions

A copper-foil electromagnetic coupler characterized by the integration of inductance and capacitance, which yields self-resonance, is proposed in this work. The absence of an additional compensation circuit in the proposed hybrid WPT system yields significant benefits, including reduced cost, lighter weight, and structural simplicity. The absence of additional compensation components and the mitigation of the skin effect collectively enhance the overall system efficiency. The relationship between the coupler's geometric parameters and system electrical parameters is analyzed and

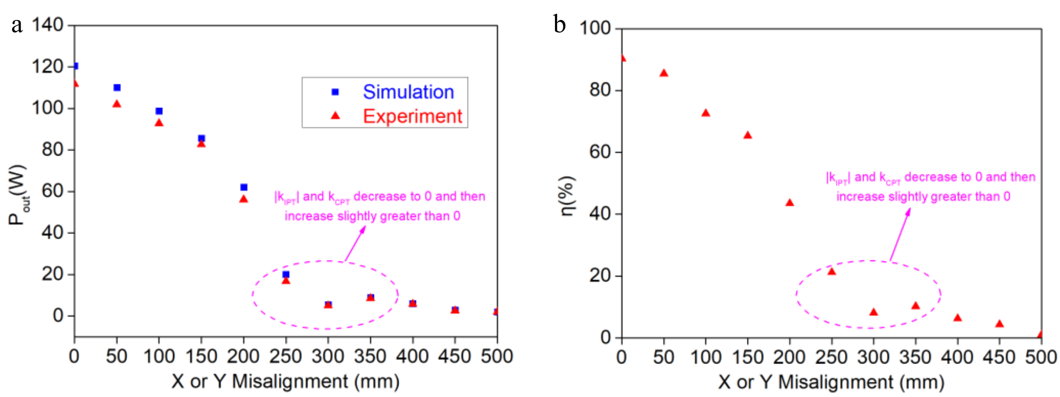

Fig. 23 (a) Test output power of the misalignment ability for this WPT system. (b) Experimental efficiency of the misalignment ability for this WPT system.

https://doi.org/10.48130/wpt-0026-0007

designed. A wide range of constant voltage output, high power factor, and ZVS conditions are achieved. An experimental device is set up with an output power of 111.84 W and an efficiency of 90.32%.

In addition, the misalignment ability of the prototype should be strengthened in the future. Because the resonant frequency is closely related to the geometric parameters of the coupler, some communication technology and control methods will be applied to this system to improve the misalignment ability. The proposed coupler and system can be well extended to the field of electric vehicles' wireless charging.

Author contributions

The authors confirm contribution to the paper as follows: study conception and design: Wu X, Li H; data collection: Wang H, Qing X; analysis and interpretation of results: Lu Z, Wang H, Feng Q; draft manuscript preparation: Wu X, Lu Z. All authors reviewed the results and approved the final version of the manuscript.

Data availability

The datasets generated during and/or analyzed in the current study are available from the corresponding author on reasonable request.

Acknowledgements

This work was supported in part by the research funds of the National Natural Science Foundation of China under Grant No. 52407003 and the Projects Supported by Scientific and Technological Research Program of Chongqing Municipal Education Commission (Grant No. KJQN202501540 and KJQN20230152).

Conflict of interest

The authors declare that they have no conflict of interest.

Dates

Received 13 November 2025; Revised 8 December 2025; Accepted 31 December 2025; Published online 2 July 2026

References

[1] Lu Z, Yan W, Huang D, Tang J, Ponci F, et al. 2024. Power flow model for medium-voltage distribution systems considering measurement and structure characteristics. *Journal of Modern Power Systems and Clean Energy* 12:571–583
[2] de Miranda CM, Pichorim SF. 2022. A three-coil wireless power transfer system using self-resonant open-bifilar coils. *AEU – International Journal of Electronics and Communications* 154:154300
[3] Tian Y, Lin Y, Tian J, Xiang L. 2021. Multi-thread sensing coil design for metal object detection of wireless power transfer systems. *Measurement* 184:109952
[4] Zhou W, Gao Q, Xiang L. 2021. Inductive–capacitive combined power transfer system and its power superposition characteristic for rail transit inspection vehicle charging. *Measurement* 185:110022
[5] Luo B, Wu H, Wang M, Wang F, Bai L, et al. 2025. Front-end parameter identification method based on Adam-W optimization algorithm for underwater wireless power transfer system. *IEEE Transactions on Power Electronics* 40:6307–6318
[6] Jin K, Zhou W. 2019. Wireless laser power transmission: a review of recent progress. *IEEE Transactions on Power Electronics* 34:3842–3859
[7] Esteban B, Sid-Ahmed M, Kar NC. 2015. A comparative study of power supply architectures in wireless EV charging systems. *IEEE Transactions on Power Electronics* 30:6408–6422
[8] Sinha S, Kumar A, Regensburger B, Afridi KK. 2019. A new design approach to mitigating the effect of parasitics in capacitive wireless power transfer systems for electric vehicle charging. *IEEE Transactions on Transportation Electrification* 5:1040–1059
[9] Li Y, Hu J, Lin T, Li X, Chen F, et al. 2019. A new coil structure and its optimization design with constant output voltage and constant output current for electric vehicle dynamic wireless charging. *IEEE Transactions on Industrial Informatics* 15:5244–5256
[10] Zhu JQ, Ban YL, Zhang Y, Cheng C, Yan Z, et al. 2019. A novel capacitive coupler array with free-positioning feature for mobile tablet applications. *IEEE Transactions on Power Electronics* 34:6014–6019
[11] Bharadwaj A, Sharma A, Reddy CC. 2023. Analytical framework of *S*-parameter-based efficiency for secondary-parallel compensation WPT system to authenticate data using VNA. *IEEE Transactions on Instrumentation and Measurement* 72:1–10
[12] Keshavarz R, Majidi E, Raza A, Shariati N. 2024. Ultra-fast and efficient design method using deep learning for capacitive coupling WPT system. *IEEE Transactions on Power Electronics* 39:1738–1748
[13] Zhou W, Tang D, Chen Z, Mai R, He Z. 2024. Nonisolation model and load virtual-grounding design method for capacitive power transfer system with asymmetric four-plate coupling interface. *IEEE Journal of Emerging and Selected Topics in Power Electronics* 12:208–218
[14] Dai J, Ludois DC. 2016. Capacitive power transfer through a conformal bumper for electric vehicle charging. *IEEE Journal of Emerging and Selected Topics in Power Electronics* 4(3):1015–1025
[15] Yao Y, Wang Y, Liu X, Lin F, Xu D. 2018. A novel parameter tuning method for a double-sided *LCL* compensated WPT system with better comprehensive performance. *IEEE Transactions on Power Electronics* 33:8525–8536
[16] Li S, Li W, Deng J, Nguyen TD, Mi CC. 2015. A double-sided LCC compensation network and its tuning method for wireless power transfer. *IEEE Transactions on Vehicular Technology* 64:2261–2273
[17] Su YG, Xie SY, Hu AP, Tang CS, Zhou W, et al. 2017. Capacitive power transfer system with a mixed-resonant topology for constant-current multiple-pickup applications. *IEEE Transactions on Power Electronics* 32:8778–8786
[18] Lian J, Qu X, Chen X, Mi CC. 2022. Design of a double-sided *LCLC*-compensated capacitive power transfer system with predesigned coupler plate voltage stresses. *IEEE Journal of Emerging and Selected Topics in Power Electronics* 10:128–137
[19] Luo B, Long T, Guo L, Dai R, Mai R, et al. 2020. Analysis and design of inductive and capacitive hybrid wireless power transfer system for railway application. *IEEE Transactions on Industry Applications* 56:3034–3042
[20] Gao X, Liu C, Zhou H, Hu W, Huang Y, et al. 2021. Design and analysis of a new hybrid wireless power transfer system with a space-saving coupler structure. *IEEE Transactions on Power Electronics* 36:5069–5081
[21] Lu F, Zhang H, Hofmann H, Mi CC. 2017. An inductive and capacitive integrated coupler and its LCL compensation circuit design for wireless power transfer. *IEEE ransactions on Industry Applications* 53:4903–4913
[22] Wu X, Mao M. 2021. A copper foil electromagnetic coupler and its wireless power transfer system without compensation. *World Electric Vehicle Journal* 12:191
[23] Badwey M, Abbasy N, Eldallal G. 2022. Extended results for a developed 10kW LC-compensated hybrid wireless power transfer system. *2022 23rd International Middle East Power Systems Conference (MEPCON), 13–15 December 2022, Cairo, Egypt*. USA: IEEE. doi: 10.1109/mepcon55441.2022.10021704
[24] Wu XY, Su YG, Hu AP, Zou LJ, Liu Z. 2020. A sleeve-type capacitive power transfer system with different coupling arrangements for rotary application. *IEEE Access* 8:69148–69159
[25] Institute of Electrical and Electronics Engineers (IEEE). 2019. IEEE standard for safety levels with respect to human exposure to electric, magnetic, and electromagnetic fields, 0 Hz to 300 GHz. *IEEE Standard C95.1-2019*. USA: IEEE. doi: 10.1109/IEEESTD.2019.8859679